RESEARCH ARTICLE

SPECIAL ISSUE: RECONSTITUTING CELL BIOLOGY

The ESCRT protein CHMP2B acts as a diffusion barrier on reconstituted membrane necks

Nicola De Franceschi[1,2,*], Maryam Alqabandi[1,2,*], Nolwenn Miguet[3], Christophe Caillat[3], Stephanie Mangenot[1,2], Winfried Weissenhorn[3,‡] and Patricia Bassereau[1,2,‡]

ABSTRACT

Endosomal sorting complexes required for transport (ESCRT)-III family proteins catalyze membrane remodeling processes that stabilize and constrict membrane structures. It has been proposed that stable ESCRT-III complexes containing CHMP2B could establish diffusion barriers at the post-synaptic spine neck. In order to better understand this process, we developed a novel method based on fusion of giant unilamellar vesicles to reconstitute ESCRT-III proteins inside GUVs, from which membrane nanotubes are pulled. The new assay ensures that ESCRT-III proteins polymerize only when they become exposed to physiologically relevant membrane topology mimicking the complex geometry of post-synaptic spines. We establish that CHMP2B, both full-length and with a C-terminal deletion (ΔC), preferentially binds to membranes containing phosphatidylinositol 4,5-bisphosphate [PI(4,5)P2]. Moreover, we show that CHMP2B preferentially accumulates at the neck of membrane nanotubes, and provide evidence that CHMP2B-ΔC prevents the diffusion of PI(4,5)P2 lipids and membrane-bound proteins across the tube neck. This indicates that CHMP2B polymers formed at a membrane neck may function as a diffusion barrier, highlighting a potential important function of CHMP2B in maintaining synaptic spine structures.

This article has an associated First Person interview with the first author of the paper.

KEY WORDS: ESCRT, CHMP2B, Dendritic spine, GUV, Membrane fusion

INTRODUCTION

Dendrites of pyramidal neurons are decorated with dendritic spines, tiny protrusions emanating from the surface of dendrites. A mature dendritic spine is shaped like a mushroom with a spherical 'head' that is connected to the dendrite through a narrow 'neck'. Each spine typically houses one postsynaptic density (PSD), the receiving site of synaptic transmissions packed with signal transduction machinery. It is generally accepted that changes in the volume of dendritic spines correlate with changes in synaptic plasticity (Yasuda, 2017). The narrow spine neck acts as a diffusion barrier

for both soluble and transmembrane proteins in order to regulate spine maturation and plasticity by compartmentalizing biochemical signaling (Adrian et al., 2014). Based on measurements of protein diffusion in the spine made by single-particle tracking *in vivo*, several proteins have been proposed to contribute to spine compartmentalization, including septins (Ewers et al., 2014) and an actin–synaptopodin complex (Wang et al., 2016).

Endosomal sorting complexes required for transport (ESCRT)-III proteins are evolutionarily conserved, and catalyze many topologically similar membrane remodeling processes including multivesicular body (MVB) biogenesis (Henne et al., 2013), enveloped virus budding (Votteler and Sundquist, 2013; Weissenhorn et al., 2013), cytokinesis (Guizetti and Gerlich, 2012; Agromayor and Martin-Serrano, 2013), plasma membrane repair (Jimenez et al., 2014), exosome biogenesis (Juan and Fürthauer, 2018) and nuclear envelope assembly (Christ et al., 2017; Olmos and Carlton, 2016). Common to all ESCRT-dependent processes is the requirement of ESCRT-III and of the ATPase VPS4 (Alonso Y Adell et al., 2016). In humans, ESCRT-III comprises IST1, two isoforms of CHMP1, two isoforms of CHMP2, CHMP3, three isoforms of CHMP4, CHMP5, CHMP6 and CHMP7 (Scourfield and Martin-Serrano, 2017). These proteins are homologous to yeast Ist1, Did2, Vps2, Vps24, Snf7, Vps60 and Vps20, respectively (CHMP7 has no yeast homologue). Although ESCRT-III proteins are expressed ubiquitously, to date, only CHMP2B has been shown to exert a confirmed specialized role in neurons (Sadoul et al., 2018) and has been linked to dendritic spine formation (Sadoul et al., 2018).

ESCRT-III proteins shuttle between a closed conformation (Muziol et al., 2006; Xiao et al., 2009) and an activated open conformation (Shim et al., 2007; Lata et al., 2008a; Zamborlini et al., 2006). Such activated CHMP proteins assemble into helical filaments, which stabilize negatively and positively curved membranes (Lata et al., 2008b; Bodon et al., 2011; Henne et al., 2012; McCullough et al., 2015; Tang et al., 2015), or loose filaments (Ghazi-Tabatabai et al., 2008; Lata et al., 2008a,b; Pires et al., 2009; Shen et al., 2014; Tang et al., 2015) that polymerize preferentially on negatively curved membranes (Lee et al., 2015) or adopt spring-like activity on flat membranes (Chiaruttini et al., 2015). In addition, active turnover of ESCRT-III polymers mediated by VPS4 seems to be required for polymer growth and membrane remodeling (Adell et al., 2017; Mierzwa et al., 2017).

Mutations in the *CHMP2B* gene lead to C-terminal CHMP2B truncations, resulting in a constitutively active protein (Skibinski et al., 2005; van der Zee et al., 2008) that is the cause of a spectrum of diseases collectively called amyotrophic lateral sclerosis/frontotemporal dementia (ALS/FTD) (Lattante et al., 2015). Silencing of CHMP2B severely inhibits spine development (Chassefeyre et al., 2015) and expression of constitutively active truncated CHMP2B impairs spine growth (Belly et al., 2010). In contrast with their usual dynamic and transient assembly in many

other processes, it has been proposed that ESCRT-III may have an additional stabilizing function during the formation, maintenance and remodeling of dendritic spines. This leads to the formation of long-lived ESCRT-III complexes containing CHMP2B (Chassefeyre et al., 2015). One hypothesis is that these stable complexes containing CHMP2B might establish diffusion barriers at the post-synaptic spine neck, regulating the concentration of receptors in spines (Chassefeyre et al., 2015), but this has not yet been verified.

Here, we set out to reconstitute *in vitro* the particular membrane geometry of a dendritic spine neck to study the effect of the CHMP2B assembly on diffusion of lipids and proteins. Since CHMP2B polymerizes *in vivo* inside the neck, it is necessary that CHMP2B is encapsulated inside a liposome and to form a membrane nanotube from the liposome mimicking the dendritic spine necks. This is technically very challenging, but necessary for two reasons: (1) membrane geometry can affect protein sorting (Prévost et al., 2015) and (2) protein assembly might be different, and thus perform different functions, when polymerizing on membranes of different geometries. Here, we used a bottom-up synthetic biology approach to investigate the function of CHMP2B in membrane tubes. We set up a novel *in vitro* assay based on laser-assisted giant unilamellar vesicle (GUV) fusion that allows encapsulation of CHMP2B while having the protein bound only on the internal side of the GUV. A nanotube can be pulled from these GUVs, allowing controlled recruitment of CHMP2B proteins into such a geometry. Our data suggest that even in the absence of other components of the ESCRT-III complexes, CHMP2B acts as a diffusion barrier at the neck of membrane geometries that resemble those present at dendritic spines.

RESULTS
CHMP2B associates preferentially with PI(4,5)P2-containing membranes
CHMP2B binds preferentially to membranes containing negatively charged lipids *in vitro*, for instance phosphatidylserine (PS) (Bodon et al., 2011). *In vivo*, the plasma membrane, in particular in dendritic spines, is enriched in phosphatidylinositol 4,5-bisphosphate [PI(4,5)P2] (Horne and Dell'Acqua, 2007). Thus, we compared binding of the active form of CHMP2B, CHMP2B-ΔC, to GUV membranes containing equimolar amounts of PS and PI(4,5)P2.

GUVs containing EPC:DOPS:DOPE:cholesterol:PI(4,5)P2:PE-Rhodamine (72.2:0:10:15:2:0.8 mol:mol) or EPC:DOPS:DOPE:cholesterol:PI(3,5)P2:PE-Rhodamine [72.2:0:10:15:2:0.8 mol:mol; or 72.2:2:10:15:0:0.8 mol:mol (i.e. no phosphatidylinositides)] (see Materials and Methods, including for definitions of lipid abbreviations) were incubated with fluorescently labeled CHMP2B (500 nM). Binding was measured by flow cytometry (Jalmar et al., 2010). We found that CHMP2B-ΔC binds to all types of GUVs with a clear preference for those containing PI(4,5)P2 (Fig. 1A; Fig. S1A). Similarly, full-length CHMP2B (CHMP2B-FL) exhibited preferential binding to PI(4,5)P2 (Fig. S1B). We also performed the same experiment by altering the amount of DOPS and PI(4,5)P2 in order to compare membranes with equal net surface charge (Visco et al., 2016). We found that CHMP2B still exhibits a preference for PI(4,5)P2 (Fig. S1C), indicating that the binding is specific. As expected, CHMP2B-ΔC, mimicking the pathological form of CHMP2B found in ALS/FTD, results in a constitutively active protein, as it significantly increases its affinity for PI(4,5)P2 as compared to CHMP2B-FL (Fig. 1B). Confocal microscopy confirmed that, due to its auto-inhibited state, CHMP2B-FL requires a longer incubation time and higher protein

concentration to reach saturation of the GUV (Fig. 1C). Both proteins seem to form a transient patchy structure on the GUV (Figs S1S, S4D), evolving into full coverage over time. In the rest of the paper, if not stated otherwise, we have used CHMP2B-ΔC and PI(4,5)P2 in the lipid composition of the vesicles.

A new assay for mimicking inverted geometry and recruitment inside a membrane neck
One method that has been developed so far for studying protein interaction with membrane geometry similar to dendritic spines involves protein encapsulation in GUVs and pulling a membrane nanotube outward, thereby creating a surface with a negative curvature accessible to proteins (Prévost et al., 2015). Both the diameter and the length of the nanotube can be controlled by micropipette aspiration and manipulation. This is in principle a powerful methodology that allows modulation of membrane curvature and tension, and detection of protein binding through fluorescence microscopy (Prévost et al., 2015), and the measurement of membrane dynamics in the nanotube through fluorescence recovery after photobleaching (FRAP) experiments (Aimon et al., 2014) or single-particle tracking (Domanov et al., 2011). However, it also presents a series of challenges, among them recruiting proteins on the internal leaflet of the GUV only.

So far, protein encapsulation in GUVs has been achieved either by inverted emulsion (Pontani et al., 2009), or by direct encapsulation during GUV growth (Prévost et al., 2015). With the first method, proteins interact only with the internal leaflet of the GUV during the full preparation process, as required, but oil contamination in the lipid bilayer affects GUV membrane dynamics and mechanics (Campillo et al., 2013). This is true in particular when negatively charged lipids such as PI(4,5)P2 lipids are present in the membrane (Prévost et al., 2015). With the second method, the protein of interest is encapsulated in GUVs containing the specific lipids required for protein–membrane interaction that are present on both membrane leaflets. GUV growth can be achieved in principle using electroformation or gel-assisted swelling on PVA or agarose (Weinberger et al., 2013; Meleard et al., 2009; Horger et al., 2009). Thus, after preparation, the proteins bind to the bilayer symmetrically and a further incubation step in high-salt buffer is necessary in order to detach the protein from the outer leaflet of the membrane (Prévost et al., 2015). Moreover, since proteins are present from the first step of the GUV growth, protein–membrane interaction kinetics cannot be assessed. With the electroformation method, we succeeded to encapsulate CHMP2B into GUVs, but unfortunately, the proteins bound to the external leaflet could not be detached from the membrane even in high-salt buffer (Fig. S2A). This is most likely due to ESCRT-III polymerization and additional insertion of the N-terminus of CHMP2B into the membrane (Buchkovich et al., 2013).

In order to overcome these technical challenges, we employed a new methodology based on laser-triggered membrane fusion (Rørvig-Lund et al., 2015) to eventually obtain CHMP2B proteins encapsulated in PI(4,5)P2-containing GUVs. The principle of our assay is the following. Two different GUVs are brought into close contact: (1) a GUV containing the protein of interest but no charged lipids or PI(4,5)P2 (thus proteins are not interacting with the membrane but are free in the lumen of the GUV) and (2) a GUV containing the PI(4,5)P2 lipids, but devoid of proteins. Both GUVs contained 0.1% (mol/mol) biotinylated lipids. Gold streptavidin-coated nanorods are bound on the surface of the GUVs; upon adsorption of focused infra-red light, the local heat triggers membrane fusion as described in Rørvig-Lund et al. (2015) and
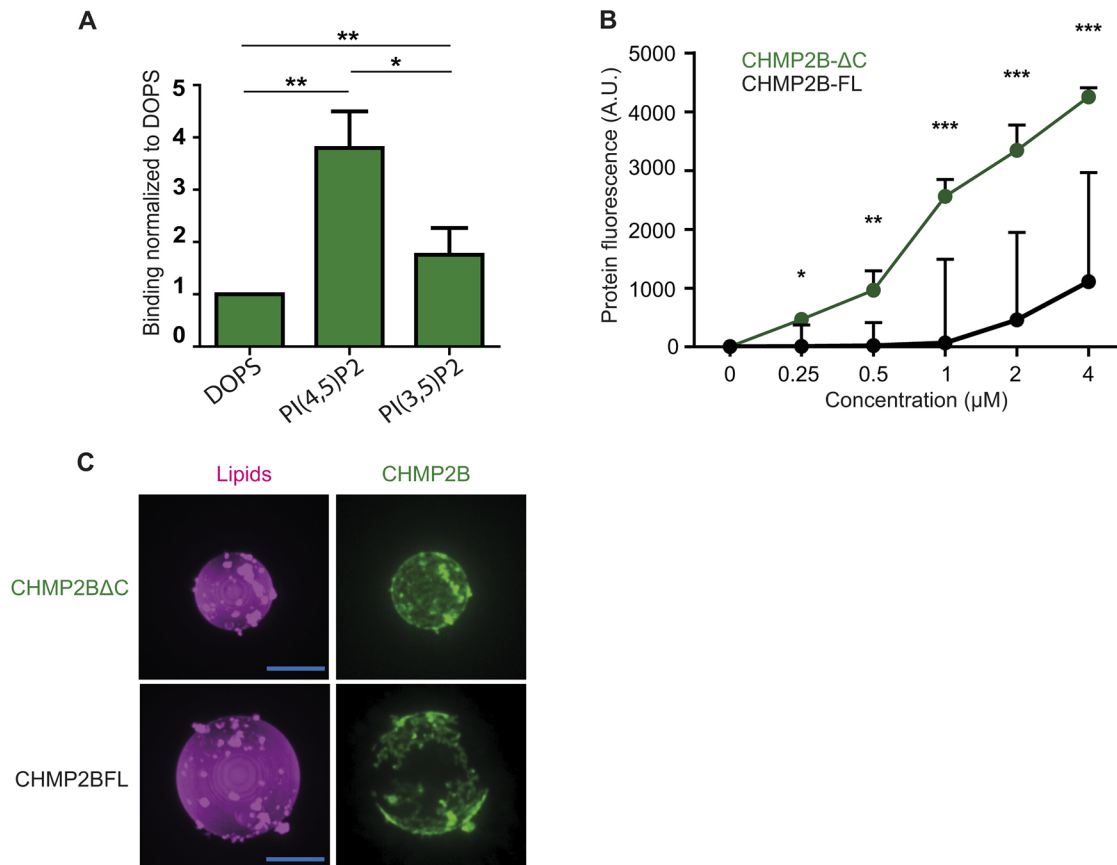
Fig. 1. Membrane binding specificity of CHMP2B. (A) Quantification (mean±s.d.) of CHMP2B-ΔC binding to GUVs containing DOPS, PI(4,5)P2 and PI(3,5)P2 by flow cytometry. Equimolar amount of DOPS, PI(4,5)P2 and PI(3,5)P2 (2% of total lipids) were used. GUVs were incubated with 500 nM CHMP2B-ΔC. **$P < 0.01$ (Student's t-test); $n=4$. (B) Titration curve (mean±s.d.) of CHMP2B-FL and CHMP2B-ΔC binding to GUVs containing 2% of PI(4,5)P2 as measured by flow cytometry. *$P < 0.05$; **$P < 0.01$; ***$P < 0.001$ (Student's t-test); $n=6$. (C) Comparison of the coverage of CHMP2B-FL and CHMP2B-ΔC polymers on GUVs. 500 nM of protein was added outside the GUV. A z-projection of the GUV is shown. Scale bars: 10 μm.

allows for lipid and content mixing. Then, CHMP2B proteins can bind to the resulting PI(4,5)P2-containing GUV (Fig. 2A).

In order to encapsulate CHMP2B-ΔC in a soluble form, we performed a polyvinyl alcohol (PVA)-gel-assisted growth for PI(4,5)P2-devoid GUVs (made of EPC only), with a protein solution in a relatively high-salt buffer (Table 1) that prevents CHMP2B polymerization. No sign of protein or lipid aggregation was visible using this method (Fig. S2B). We encapsulated CHMP2B at ≈250 nM (Fig. S2C, see Materials and Methods section), which would drop to ≈125 nM after fusion of two GUVs of equal size, which is in the range of physiological concentration of ESCRT-III proteins estimated in yeast (Teis et al., 2008). For the charged GUVs, we used the lipid composition described in Table 1, with 10% (mol/mol) PI(4,5)P2, which resembles the inner leaflet of the plasma membrane (Prévost et al., 2015) [EPC:DOPS:DOPE: cholesterol:PI(4,5)P2:PE-Rhodamine (54.2:10:10:15:10:0.8 mol: mol)] and which triggers CHMP2B binding. In order to link the streptavidin-coated nanorods to the GUV surface as well as the beads used for tube pulling, this mixture was supplemented with 0.1% (mol/mol) biotinylated lipids. The PI(4,5)P2-containing vesicles were prepared in a low-salt buffer, so that upon fusion and content mixing, CHMP2B could polymerize at optimal salt concentration (Table 1). Moreover, since PVA-assisted growth results in GUVs with a large size polydispersity, the GUVs to be fused can be selected based on their relative size, in order to achieve the desired salt, CHMP2B and PI(4,5)P2 amount in the final fused

vesicle. This allows exquisite control over the experimental conditions.

Practically, GUVs are incubated with streptavidin-coated gold nanorods, which interact with the biotinylated lipids present in the external leaflet of the membrane. These nanorods absorb infrared light. Subsequently, the two populations of GUVs are mixed in the observation chamber, along with 3 μm streptavidin-coated beads that allow pulling a nanotube from GUVs. The two GUVs are held by micropipettes, while a third micropipette holds the streptavidin-coated bead. A membrane nanotube is pulled using the streptavidin-coated bead, the two GUVs are brought in contact, and the infrared laser (λ=1064 nm) is turned on, focused at the interface between the two membranes through the objective, which very rapidly induces fusion (Movie 1). We first tested this system by encapsulating Alexa Fluor 647-labeled fibronectin in a GUV containing a green lipid dye (BODIPY FL C5-ganglioside GM1) and by fusing it with GUVs containing a red lipid dye (Rhodamine–DOPE) (Fig. 2B). Upon fusion, we observed instantaneous content mixing, while lipid mixing required a few seconds to be completed. Importantly, we observed that the lipid nanotube was stable during the fusion event; moreover, complete lipid mixing indicates that the fusion protocol does not result in membrane defects that could impair free diffusion of lipids in the membrane plane. In order to ascertain whether the interior of the nanotube is directly connected to the GUV lumen after fusion, we encapsulated the I-BAR domain of IRSp53 (denoted I-BAR-IRSp53; IRSp53 is also known as BAIAP2),
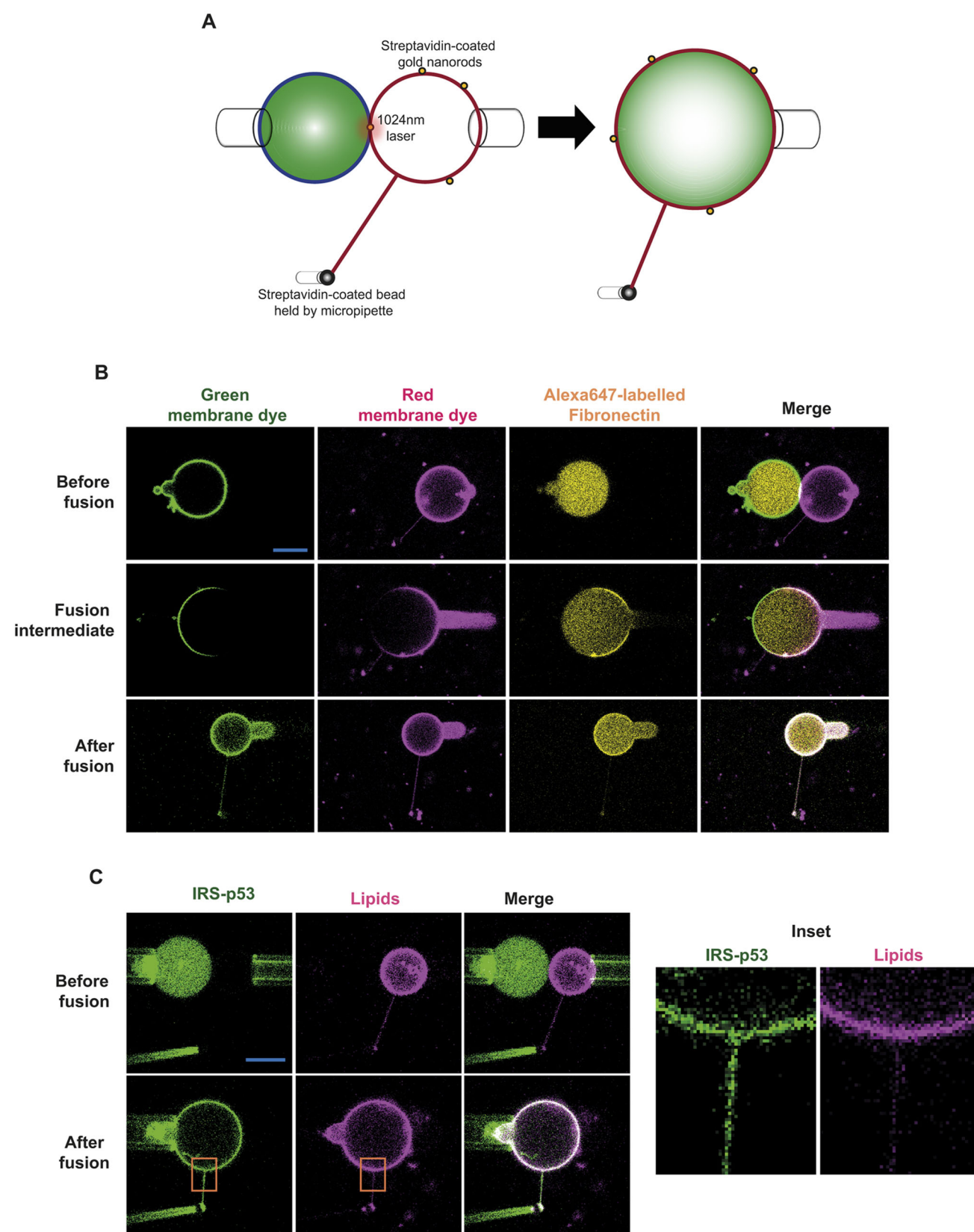
Fig. 2. Protein reconstitution on negatively curved membranes by GUV fusion. (A) Schematic illustrating the experimental assay based on GUV fusion. A GUV containing PI(4,5)P2 is depicted in red, while soluble protein encapsulated in an EPC GUV is indicated in green. (B) Fusion of a GUV containing the green lipid BODIPY FL C5-ganglioside and soluble Alexa Fluor 647-labeled fibronectin (yellow) in the lumen with a GUV containing Rhodamine–DOPE lipids (magenta). A fusion intermediate, in which full lipid mixing is not yet completed, is shown. The fusion intermediate is typically captured 2 s after fusion. Scale bar: 10 µm. (C) Reconstitution of IRSp53 inside a membrane nanotube after GUV fusion. Insets show protein enrichment inside the tube as compared to the lipid signal after fusion. Scale bar: 10 µm.

Table 1. Buffer and lipid compositions used in this study

	Growth buffer for PI(4,5)P2 vesicles	Growth buffer for protein encapsulation	External buffer
NaCl (mM)	20	70	70
Tris (mM)	25	25	50
Sucrose (mM)	180	80	
Glucose (mM)			55
Osmolarity (mOsm)	245	245	245

	Lipid composition for PI(4,5)P2 vesicles	Lipid composition for protein encapsulation
Egg PC (mol%)	54.7	100
DOPS	10	
DOPE	10	
PI(4,5)P2	10	
Cholesterol	15	
DSPE–PEG2000–Biotin	0.2	
18:1 Liss-Rhodamine–PE	0.1	

which binds preferentially to negatively curved membranes, and thus is enriched inside the membrane nanotube (Prévost et al., 2015). I-BAR-IRSp53 was encapsulated in GUVs composed of EPC, keeping the protein in the GUV lumen (Fig. 2C). The second population of vesicles contained PI(4,5)P2, which recruits I-BAR-IRSp53 to the membrane (Prévost et al., 2015). A tube was pulled from the protein-free GUV prior to fusion. As expected, we found that I-BAR-IRSp53 was enriched in the nanotube after fusion (Fig. 2C). No loss of GUV content could be detected outside the GUV upon fusion.

CHMP2B localizes at the neck of membrane tubes

Having established the experimental conditions for encapsulating proteins and having them bind to the interior of a tube neck, we investigated how CHMP2B-ΔC interacts with a membrane with such a geometry mimicking a dendritic spine. Upon fusion, CHMP2B-ΔC binds to the membrane instantaneously. In Fig. 3A, we show an image taken just after fusion where lipids had not yet equilibrated between both GUVs but where CHMP2B proteins were already bound to the PI(4,5)P2-rich part of the GUV. However, over the course of a few seconds the organization of the CHMP2B-ΔC polymer drastically changed, and the protein that initially exhibited a diffuse binding to the membrane rearranged forming bright clusters (Fig. 3B; Movie 2). These clusters freely diffused on the membrane, but had a strong tendency to localize to the base of the neck of membrane nanotubes (Fig. 3B; Movie 3). Since the membrane nanotube diameter can be deduced from the measurement of the lipid fluorescence as previously established (Sorre et al., 2012), we could show that CHMP2B-ΔC clusters display a preference for narrower membrane nanotubes (Fig. 3C). Occasionally, GUV fusion results in the formation of multiple nanotubes due to unspecific adhesion of the GUV membrane to the micropipettes or to the surface of the chamber. The striking preference of CHMP2B-ΔC for the neck region is exemplified in one of these examples, in which three nanotubes are decorated with CHMP2B-ΔC clusters at their neck (Fig. S3A). In similar experimental conditions, CHMP2B-FL exhibits weak or no

binding upon fusion and small clusters are only rarely observed, in line with its lower affinity for PI(4,5)P2 (Fig. S3B). However, whenever such clusters were formed, they also preferentially localized to the neck region (Fig. 3D). Thus, the localization of CHMP2B at dendritic spines seen in vivo (Chassefeyre et al., 2015) might be due to an intrinsic tendency of this protein to localize to the particular membrane geometry of a tube neck. In order to reproduce on the outside of GUVs similar binding conditions to that on the inside upon the fusion, we incubated GUVs with either CHMP2B-ΔC or CHMP2B-FL at low concentration (30 nM and 200 nM, respectively, to compensate for different membrane binding affinity) for a short time (5 min). We observed formation of mobile clusters (Movie 4), very similar to those formed inside GUVs upon fusion (Fig. 3E). These clusters appear to be able to locally deform the membrane into a shape reminiscent of a neck, which invariably points towards the interior of the GUV (Fig. 3F), creating a membrane topology that corresponds to that obtained by tube pulling (Fig. 3B,D).

However, the peculiar localization of CHMP2B does not provide any clue about how it can affect membrane dynamics. We therefore studied the diffusion of different membrane components first on flat membranes coated with CHMP2B-ΔC, next in tubes where CHMP2B-ΔC interacts at the neck.

CHMP2B polymerization blocks diffusion on flat membranes

We used FRAP to study dynamics of some membrane components on GUVs when CHMP2B-ΔC is bound to the external leaflet of GUVs, for sake of simplicity. We performed these experiments using a protein concentration higher than the physiological one, in order to be able to investigate CHMP2B properties at the mesoscale in the condition of full GUV coverage. First, when incubating GUVs with CHMP2B-ΔC and rinsing after binding to remove unbound protein left in solution, we observed that no significant recovery of CHMP2B-ΔC occurred after photobleaching even after 6 min and beyond (Fig. 4A; Table 2). This indicates that once assembled, CHMP2B-ΔC polymers do not diffuse on the GUV surface, and probably form an inter-connected structure. Note that the absence of recovery of CHMP2B-FL is indistinguishable from that of CHMP2B-ΔC (Fig. S4C, Table 2), indicating that this property is intrinsic to the CHMP2B polymer and not only a result of the C-terminal truncation. We next performed FRAP experiments on GUVs at lower membrane CHMP2B-ΔC and CHMP2B-FL coverage, to check if this property persists. We did not measure any fluorescence recovery over a long period of time (at least 3 min), but we observed that the proteins form a static interconnected structure at the GUV surface, which explains the absence of fluorescence recovery (Movie 5). At higher protein coverage, GUVs appear homogenously covered with CHMP2B proteins at optical resolution, but the FRAP results indicate that they retain a connected structure.

We compared this behavior with assembly of other ESCRT-III proteins, namely CHMP2A-ΔC together with CHMP3. These proteins have also been shown to form polymers when incubated together (Lata et al., 2008a,b). In contrast with CHMP2B-ΔC, we observed fluorescence recovery in less than 2 min, showing that these co-polymers freely diffuse on the membrane (Fig. 4A; Table 2). This was not due to a difference in protein density at the GUV surface, as the density of CHMP2A was in fact about six times higher than that of CHMP2B (Fig. S4B,C; see Materials and Methods section for more details). When performing an analogous FRAP experiment on a CHMP2B-ΔC–CHMP2A-ΔC–CHMP3-FL co-polymer, CHMP2B appears to have a dominant effect, blocking the diffusion of the other ESCRT proteins (Fig. S4D).
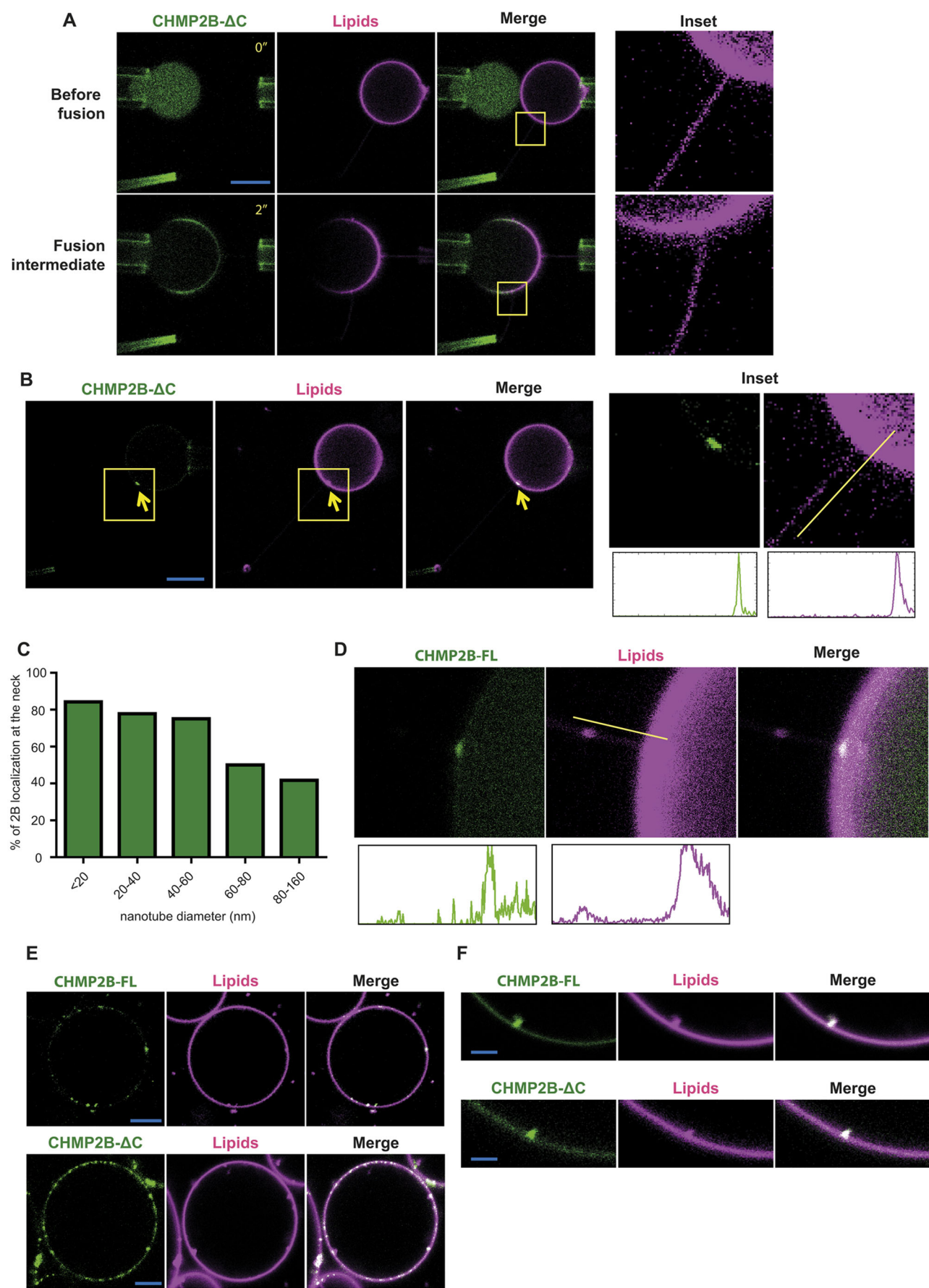
Fig. 3. See next page for legend.

Fig. 3. CHMP2B localization at the neck of membrane nanotube upon GUV fusion. (A) Fusion of GUVs containing CHMP2B-ΔC (left) and PI(4,5)P2 (right). Insets show that the membrane nanotube is preserved upon fusion. The fusion intermediate is typically captured 2 s after fusion. (B) CHMP2B-ΔC cluster localization at the base of the membrane nanotube after fusion. Insets show a magnification of the neck region. The lipid signal has been increased in order to visualize the nanotube. The arrow indicates the position of the neck. An intensity profile of the nanotube along the direction indicated by the yellow line is shown for both the protein and the lipid channels. (C) Quantification (mean) of the stable CHMP2B-ΔC localization at nanotube neck. Quantification of 19 nanotubes of variable diameters from 11 GUVs from three independent GUV preparations. For each nanotube diameter, *n* measurements have been obtained: <20 nm, *n*=19; 20–40nm, *n*=9; 40–60 nm, *n*=8; 60–80 nm, *n*=4, 80–160 nm, *n*=12. The percentage corresponds to the fraction of tube necks, over *n*, exhibiting a CHMP2B cluster, for each tube diameter range. (D) A CHMP2B-FL cluster localizing at the base of a membrane nanotube after fusion. Note the lower signal of the cluster as compared to the residual protein left inside the GUV that is not bound to the membrane, indicating lower affinity of the membrane for CHMP2B-FL as compared to CHMP2B-ΔC. An intensity profile of the nanotube along the direction indicated by the yellow line is shown for both the protein and the lipid channels. (E) Clusters resulting from incubation of a GUV with either CHMP2B-ΔC or CHMP2B-FL added on the outside, at a concentration of 30 nM and 200 nM, respectively. Incubation time: 5 min. (F) Magnified images of clusters resulting from incubation of GUV with either CHMP2B-ΔC or CHMP2B-FL. Scale bars: 10 μm (A,B,D,E); 5 μm (F).

We next wondered whether the connected network structure formed by CHMP2B could likewise block diffusion of membrane-bound and transmembrane proteins. We measured the diffusion of Alexa Fluor 561-labeled streptavidin bound to biotinylated lipids to mimic membrane-bound protein on the surface of GUVs and found that the CHMP2B-ΔC polymer indeed completely blocks streptavidin diffusion (Fig. 4B, Table 2). In contrast, recovery took place when the GUV was covered with CHMP2A-ΔC–CHMP3 co-polymers. We next investigated the ability of CHMP2B-ΔC to block diffusion of transmembrane proteins reconstituted in GUVs. Since ion channels play a crucial role in neuron function, we chose to study KvAP, a bacterial member of the voltage-gated ion channel family, as a model of ion channel diffusion. Indeed, members of the Kv family localize in dendrites or axon (Shah et al., 2010). Upon photobleaching, we observed no recovery of KvAP after ~4 min when the exterior of the GUV was covered by CHMP2B-ΔC polymer (Fig. 4C, Table 2).

Prompted by these findings, we wondered whether CHMP2B could also act as a diffusion barrier for PI(4,5)P2 lipids. Analogous FRAP experiments revealed that, at the mesoscale, CHMP2B-ΔC acts as a weak barrier for PI(4,5)P2, being able to slow down its diffusion as compared to the CHMP2A–CHMP3 co-polymer, without completely inhibiting it (Fig. 4D, Table 2).

Since CHMP2B-ΔC forms a diffusion barrier for proteins on quasi-flat membranes and since it is found preferentially at tube necks, we next investigated whether CHMP2B could function as a diffusion barrier at a nanotube neck.

CHMP2B blocks the diffusion of membrane-bound proteins in the neck

In order to investigate the putative role of CHMP2B as a diffusion barrier at necks, we co-encapsulated Alexa Fluor 647-labeled CHMP2B-ΔC with Alexa Fluor 488-labeled streptavidin in EPC vesicles. Co-encapsulation did not result in any sign of aggregation (Fig. S5). Upon fusion with GUVs containing 10% (mol/mol) PI(4,5)P2 and 0.2% (mol/mol) biotinylated lipids, both proteins bound, with little residual unbound protein left in the GUV lumen; moreover streptavidin was also found in the nanotube. Interestingly, CHMP2B-ΔC clusters seemed to trap membrane-bound streptavidin,

as the two signals often overlapped (Fig. 5A). Upon bleaching of streptavidin present in the nanotube, only a limited recovery could be detected when a CHMP2B-ΔC cluster was present at the neck. As a control, we do observe full recovery when no CHMP2B-ΔC clusters happened to localize at the neck (Fig. 5B, Table 2; Movie 6). Thus, the ability of CHMP2B-ΔC to block diffusion of membrane-bound proteins at the mesoscale is conserved at the scale and in the geometry of a membrane neck. We next wondered whether CHMP2B-ΔC could also block PI(4,5)P2 diffusion through the neck. Upon fusion and bleaching, we could observe recovery of PI(4,5)P2 in the nanotube in the absence of the CHMP2B-ΔC signal at the neck. In striking contrast with analogous measurements performed on GUVs at the mesoscale (Fig. 4D), we observed that CHMP2B-ΔC clusters strongly impaired PI(4,5)P2 diffusion in the nanotube through the neck (Fig. 5C, Table 2), suggesting a clear role for membrane geometry in this process.

DISCUSSION

Following a bottom-up synthetic biology approach, we have developed a novel system to reconstitute and study protein interaction inside membrane tubes. Previously described protocols to encapsulate soluble proteins inside GUVs could not be employed because of the very strong interaction of ESCRT-III proteins with either the outer or inner membrane of GUVs and of the difficulty to detach them from the outer membrane due to their propensity to polymerize on membranes. In our newly developed protocol, we first encapsulate soluble monomeric ESCRT-III proteins into GUVs with lipid compositions that impede their interaction with membranes. Such GUVs with a free reservoir of ESCRT-III in their lumen can then be fused to GUVs with a lipid composition that enables ESCRT-III interaction, and/or with GUVs that have tubes pulled with defined diameters (Prévost et al., 2015). Our protocol is broadly applicable and particularly suited to study proteins with affinity for negatively curved membranes, but exhibiting strong and irreversible binding to membranes, which are intractable with other available methods. In addition, with our method, multiple fusion events can be performed, potentially allowing the study of sequential protein recruitment in an otherwise inaccessible membrane surface. It could be used to study the assembly of other ESCRT-III proteins, and potentially scission, in the presence of ATP in a geometry mimicking that of cellular or viral buds. Several other cellular structures exhibit membrane geometries resembling membrane tubes, such as the base of dendritic spines, filopodia, tunneling nanotubes or cilia, and the neck structures of budding vesicles and viruses to name a few, and our methodology could be very useful to develop biomimetic approaches.

We show that CHMP2B binding at equal surface charge density is ~2.5 times higher in the presence of PI(4,5)P2 as compared to with DOPS (Fig. S1C) indicating a specific interaction with PI(4,5)P2. CHMP2B is the result of gene duplication from the ancestral yeast Vps24 gene (Leung et al., 2008), and the ESCRT-III complex acquired a series of new functions in *Homo sapiens* as compared to *Saccharomyces cerevisiae*. Interestingly, CHMP2B has been implicated in all these newly acquired functions, which occur either at the plasma membrane or at the nuclear envelope, both of which are enriched in PI(4,5)P2 (Di Paolo and De Camilli, 2006; Garnier-Lhomme et al., 2009). Furthermore, C-terminally truncated CHMP2B has a stronger binding affinity for PI(4,5)P2-containing membranes than its full-length version (Fig. 1B), consistent with the proposal that C-terminal deletions facilitate the activation of ESCRT-III proteins (Shim et al., 2007; Lata et al., 2008a,b)
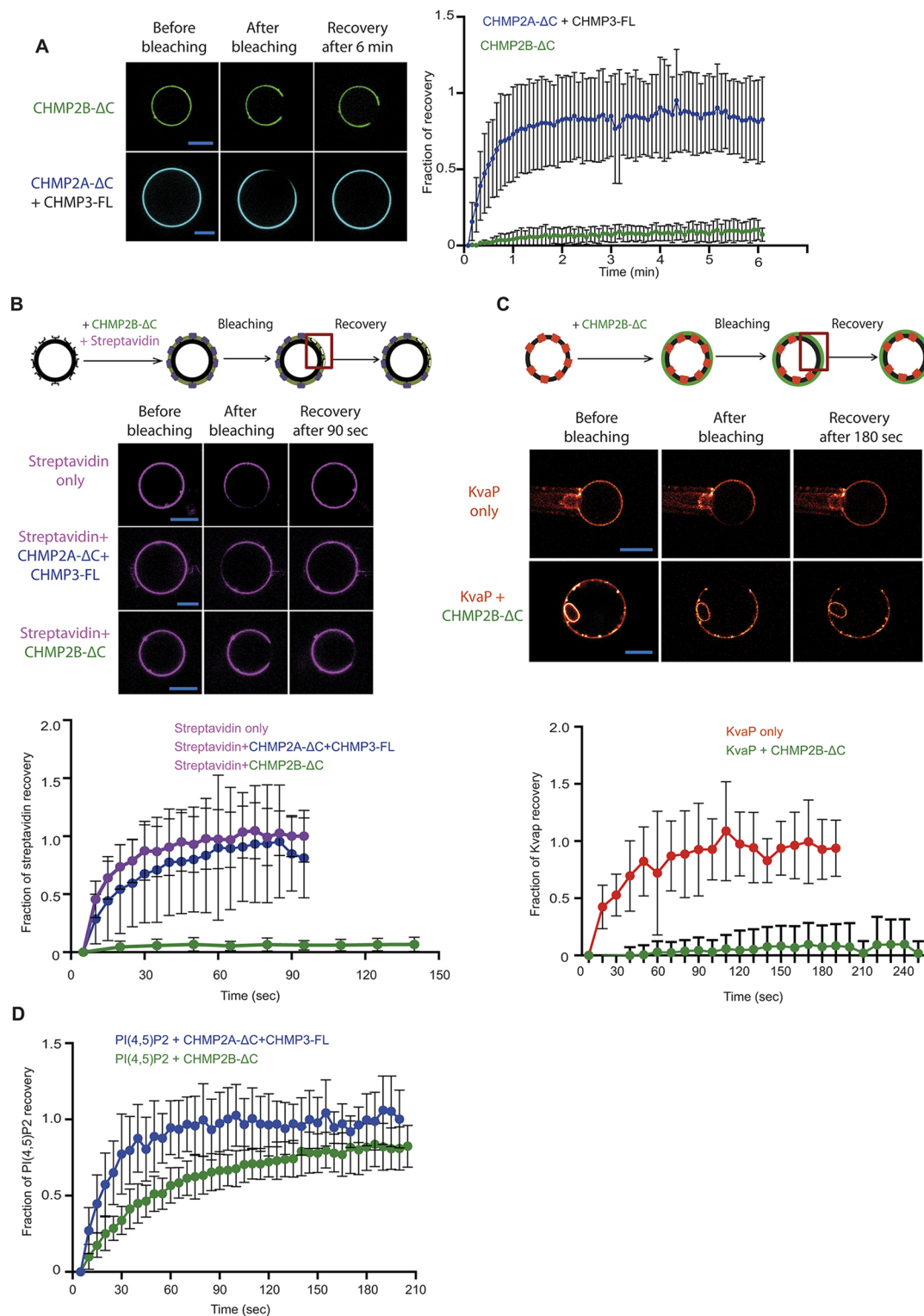
Fig. 4. CHMP2B acts as a diffusion barrier for membrane components on GUV surface. (A) FRAP experiment on CHMP2B-ΔC (upper panels) and CHMP2A-ΔC+CHMP3-FL (lower panels) bound to the external leaflet of GUVs. All proteins were mixed with GUVs at a concentration of 500 nM. Soluble proteins in the GUV external solution have been removed by dilution. Protein polymers were bleached and protein recovery measured over time. One confocal plane is shown. Results are mean±s.d. from 46 FRAP experiments from three independent GUV preparations. (B) Streptavidin recovery after photobleaching on biotinylated GUVs. GUVs were pre-incubated with either CHMP2A-ΔC+CHMP3-FL or CHMP2B-ΔC. All proteins were mixed with GUVs at a concentration of 500 nM. A negative control without pre-incubation with ESCRT proteins is also shown. One confocal plane is shown. Results are mean±s.d. from 28 FRAP experiments measured from two independent GUV preparations. (C) Alexa Fluor 488-labeled KvaP recovery after photobleaching on GUVs. GUVs were pre-incubated with CHMP2B-ΔC at 500 nM. A negative control without pre-incubation with CHMP2B-ΔC is shown. Results are mean±s.d. from 35 FRAP experiments measured from three independent GUV preparations. (D) TopFluo-PI(4,5)P2 recovery after photobleaching on GUVs. GUVs were pre-incubated with CHMP2B-ΔC at 500 nM. A negative control without pre-incubation with CHMP2B-ΔC is shown. Results are mean±s.d. from 31 FRAP experiments measured from two independent GUV preparations. Scale bars: 10 µm.

Table 2. $t_{1/2}$ and immobile fraction for FRAP experiments presented in this study

Figure panel	Protein	$t_{1/2}$ (s)	Immobile fraction (%)
Fig. 4A	CHMP2A-ΔC+CHMP3-FL	17	16
	CHMP2B-ΔC	60	90
Fig. 4B	Streptavidin	15	0
	Streptavidin+CHMP2A-ΔC+ CHMP3-FL	20	10
	Streptavidin+CHMP2B-ΔC	20	94
Fig. 4C	KvaP	15	5
	KvaP+CHMP2B-ΔC	70	93
Fig. 4D	PI(4,5)P2+CHMP2A-ΔC+ CHMP3-FL	12	0
	PI(4,5)P2+CHMP2B-ΔC	30	18
Fig. 5B	Streptavidin	15	0
	Streptavidin+CHMP2B-ΔC	10	87
Fig. 5C	PI(4,5)P2	27	41
	PI(4,5)P2+CHMP2B-ΔC	25	90
Fig. S4	CHMP2B-ΔC	30	95
	CHMP2B-FL	40	98

required for polymerization (McCullough et al., 2015; Tang et al., 2015).

Genetic mutations in *CHMP2B* lead to C-terminally truncated, and thus 'activated' CHMP2B, and have a link to frontotemporal dementia (FTD) (Skibinski et al., 2005). Indeed, CHMP2B concentrates beneath the perisynaptic membrane of dendritic spines (Lendvai et al., 2003) and CHMP2B mutations linked to FTD or expression of C-terminally truncated CHMP2B decrease the proportion of large spines with mushroom morphology significantly, indicating an important morphological role for CHMP2B in dendritic spine formation (Belly et al., 2010).

Spine neck diameters are quite variable, and range from 80 to 510 nm as imaged in pyramidal cells from the mouse visual cortex (Arellano et al., 2007). Here, we pulled membrane tubes with diameters ranging from 20 nm to 160 nm, and showed that CHMP2B concentrates at the neck of the tubes and more efficiently at the neck of small diameter nanotubes (20 nm). Obtaining nanotubes with larger diameter is technically challenging due to the membrane tension that the GUV usually acquires after fusion.

We show that not only is CHMP2B able to localize at the nanotube neck, but it can also deform membranes into a shape reminiscent of a neck. Once localized at the neck, CHMP2B prevents diffusion of PI(4,5)P2 and membrane-bound streptavidin. Although our approach could in principle be used to fuse GUVs with reconstituted transmembrane proteins, the intrinsic fragility and the limited surface fraction of proteins that can be achieved, and thus the low fluorescent signal of proteoGUVs, hindered such experiments.

Although the diffusion of membrane-associated proteins and lipids has been investigated in cells (Trimble and Grinstein, 2015; Hu et al., 2010; Schlimpert et al., 2012), the underlying molecular mechanisms regulating this process are still not fully understood. *In vitro*, an actin meshwork artificially tethered to a membrane has been shown to control diffusion of membrane-bound proteins (Heinemann et al., 2013). However, this study was performed on flat membranes. To the best of our knowledge, we are providing the first example of modulation of proteins and lipids diffusion by a protein polymer on an inverted and curved membrane geometry.

Our data further suggest that the presence of CHMP2B at the neck of a membrane tube might stabilize the neck architecture and act as a diffusion barrier for both membrane-associated proteins and lipids.

This is consistent with the observation that CHMP2B-containing plasma membrane tubes formed *in vivo* exclude plasma membrane receptors due to the tight packing of the CHMP2B helical scaffold against the tube membrane (Bodon et al., 2011). Because of the tight interaction of ESCRT-III polymers with membranes (McCullough et al., 2015; Tang et al., 2015), ESCRT-III polymer assemblies may function in general as a diffusion barrier.

Although the turnover of ESCRT-III complexes is rather fast during budding (Baumgärtel et al., 2011; Jouvenet et al., 2011), CHMP2B-containing ESCRT-III complex(es) that stabilize dendritic spines likely have a longer half life. Notably, dendritic spine architecture is maintained over long periods ranging from hours and days during their development to life-long structures (Grutzendler et al., 2002; Trachtenberg et al., 2002; Yang et al., 2009), with the possibility of rapid changes in spine shape and size occurring upon external stimuli (Lendvai et al., 2003). Here, we used C-terminally truncated CHMP2B, which retains the capacity to assemble at tube necks and function as a diffusion barrier. Thus, the genetic CHMP2B mutations leading to FTD (Skibinski et al., 2005) and aberrant spine architecture in cultured neurons (Belly et al., 2010) do not affect CHMP2B function on membranes but most likely interfere with VPS4-mediated ESCRT-III CHMP2B polymer remodeling due to the lack of the VPS4-interacting MIM [microtubule interacting and transport domain (MIT) interacting motif] (Henne et al., 2012). This supports the notion that ESCRT-III CHMP2B remodeling may be required to maintain dendritic spine architectures. In a speculative model, the assembly of CHMP2B at membrane tube necks, which resembles those present at dendritic spines, would tightly interact with the membrane and thereby block the diffusion of membrane-associated proteins and PI(4,5)P2 into the spine. This might help to maintain specific spine structure for a limited time before they are remodeled themselves in order to change plasticity (Fig. 5D).

MATERIALS AND METHODS
Recombinant proteins
CHMP3-FL was expressed in *Escherichia coli* BL21 cells for 3 h at 37°C (Muziol et al., 2006). Briefly, cells were harvested by centrifugation (4000 ***g*** for 20 min at 4°C) and the bacterial pellet was resuspended in 50 ml of binding buffer A (20 mM Bicine pH 9.3, 300 mM NaCl, 5 mM imidazole, 1% CHAPS/1 mM PMSF). The bacteria were lysed by sonication and CHMP3-FL was purified by Ni^{2+} chromatography. A final gel filtration chromatography step was performed in buffer B (20 mM Hepes pH 7.6, 150 mM NaCl). CHMP2A-ΔC was expressed as MBP fusion protein in *Escherichia coli* BL21 cells (Lata et al., 2008a,b) for 1 h at 37°C. Cells were harvested by centrifugation (4000 ***g*** for 20 min at 4°C) and the bacterial pellet was resuspended in 50 ml of binding buffer C (20 mM Hepes pH 7.6, 300 mM NaCl, 300 mM KCl). The bacteria were lysed by sonication, and CHMP2A-ΔC was purified on an amylose column. CHMP2A-ΔC was labeled overnight at 4°C with Alexa Fluor 405 NHS Ester (Thermo Fisher Scientific) using a molar ratio (Alexa Fluor:protein) of 2:1. A final gel filtration chromatography step was performed in a buffer B. CHMP3-FL and CHMP2A-ΔC were concentrated to 20 μM, and immediately frozen in liquid nitrogen with 0.1% of methyl cellulose (Sigma-Aldrich) as cryo-protectant. All aliquots were kept at −80°C prior to experiments.

CHMP2B-ΔC contains amino acids 1–154, and a C-terminal SGSC linker for cystein-specific labeling. CHMP2B-FL contains the full-length sequence with a C-terminal SGSC linker for cystein-specific labeling. Both proteins were expressed in *Escherichia coli* BL21 cells for 4 h at 37°C. Cells were lysed by sonication in buffer D [50 mM Tris-HCl pH 7.4, 1 M NaCl, 10 mM DTT and protease inhibitor (Complete EDTA free, Roche) at the concentration indicated by the manufacturer] and the soluble fraction was discarded after centrifugation (50,000 ***g***, 20 min, 4°C). The pellet was washed three times with buffer E (50 mM Tris-HCl pH 7.4, 2 M urea, 2% Triton X-100 and
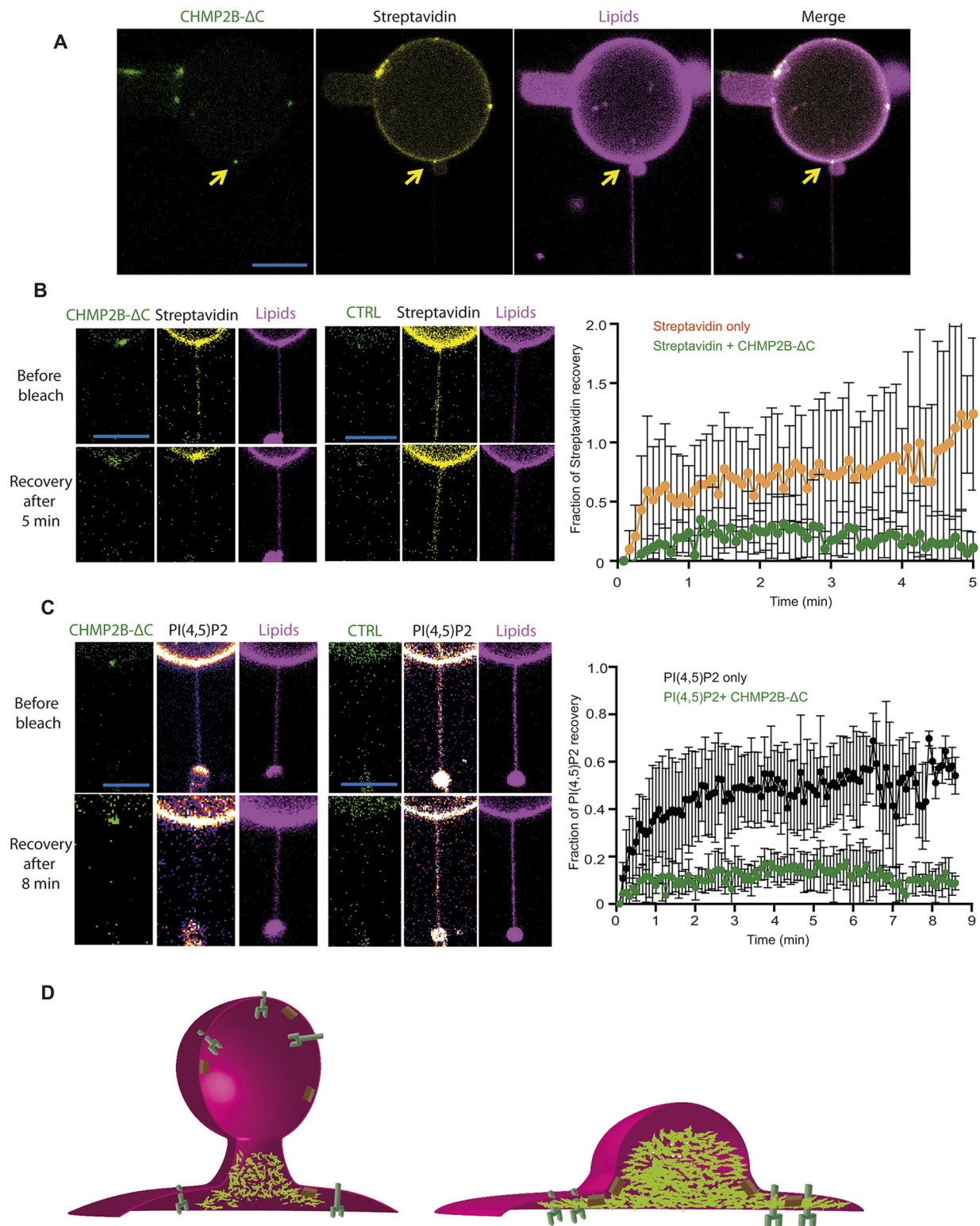
Fig. 5. CHMP2B acts as a diffusion barrier for membrane components at a nanotube neck. (A) A representative example of GUV obtained after fusion between a EPC vesicle containing soluble streptavidin and CHMP2B-ΔC, and a PI(4,5)P2 vesicle containing biotinylated lipids. Arrows indicate the position of the neck. (B) Recovery of Alexa-Fluor-488-labeled streptavidin after photobleaching on a nanotube. A negative control in which a CHMP2B-ΔC cluster is not present at the neck, is shown. Results are mean±s.d. from 10 FRAP events measured from two independent experiments. (C) TopFluo-PI(4,5)P2 recovery after photobleaching on nanotube. A negative control in which a CHMP2B-ΔC cluster is not present at the neck, is shown. Results are mean±s.d. from 22 FRAP events measured from two independent experiments. (D) Speculative model representing the putative physiological and pathological role of CHMP2B in dendritic spine. In normal conditions (left panel) CHMP2B acts as a membrane stabilization factor and regulator of diffusion, in concert with Alix and CHMP4B. The constitutively active form of CHMP2B tends to accumulate at the base of dendritic spine and is less prone to remodeling by the action of VPS4, which is necessary for spine physiology. This causes accumulation of an aberrant CHMP2B polymer that impairs diffusion of membrane components and does not allow remodeling. Scale bars: 10 μm

2 mM β-mercaptoethanol). The last wash was performed in absence of urea and Triton X-100. The extraction of CHMP2B was performed in 50 mM Tris-HCl pH 7.4, 8 M guanidine, 2 mM β-mercaptoethanol overnight at 4°C. After centrifugation (50,000 g, 20 min, 4°C), CHMP2B was purified by Ni^{2+}-chromatography in buffer F (50 mM Tris-HCl pH 7.4, 8 M urea). The protein was eluted in 50 mM Tris-HCl pH 7.4, 8 M urea, 2 mM β-mercaptoethanol, 250 mM imidazole. Refolding was performed by rapid dilution of CHMP2B into buffer G (50 mM Tris-HCl pH 7.4, 200 mM NaCl, 2 mM DTT, 50 mM L-glutamate, 50 mM L-arginine) and a final concentration of 2 μM. CHMP2B was concentrated by passing it over a Ni^{2+} column in buffer H (50 mM Tris-HCl pH 7.4, 200 mM NaCl) and eluted in buffer I (50 mM Tris-HCl pH 7.4, 300 mM NaCl, 250 mM imidazole). CHMP2B was labeled overnight at 4°C with Alexa Fluor 488 C5 Maleimide (Thermo Scientific) with a molar ratio (Alexa Fluor:protein) of 2:1. A final gel filtration chromatography step was performed on a superdex75 column in buffer J (50 mM Tris-HCl pH 7.4, 100 mM NaCl). Both CHMP2B-FL and CHMP2B-ΔC were concentrated to 20 μM, and immediately frozen in liquid nitrogen with 0.1% of methyl cellulose (Sigma-Aldrich) as a cryo-protectant. All aliquots were kept at −80°C prior to experiments

Streptavidin was purchased from Sigma-Aldrich and labeled using Alexa Fluor 488 5-SDP Ester (Thermo Fisher Scientific). Excess label was removed by extensive dialysis. β-casein from bovine milk (>99%) was purchased from Sigma-Aldrich (France). Fibronectin was purchased from Sigma-Aldrich and labeled using Alexa Fluor647-SDP Ester (Thermo Fisher Scientific). Excess label was removed by extensive dialysis.

Lipid reagents
1,2-dioleoyl-sn-glycero-3-phosphatidylcholine (DOPC), 1,2-dioleoyl-sn-glycero-3-phospho-L-serine (DOPS), 1,2-dioleoyl-sn-glycero-3-phosphatidylethanol-amine (DOPE), cholest-5-en-3β-ol (cholesterol), (1,2-dioleoyl-sn-glycero-3-phospho-(1′-myo-inositol-3′,5′-bisphosphate) [PI(3,5)P2], L-α-phosphatidylinositol-4,5-bisphosphate [PI(4,5)P2], Egg L-α-phosphatidylcholine [EPC] and L-α-phosphatidylethanolamine-N-(lissamine Rhodamine B sulfonyl) (egg PE–Rhodamine) were purchased from Avanti Polar Lipids. Stock solutions of lipids were dissolved in chloroform at a concentration of 10 mg ml^{-1}, except for PI(4,5)P2, which was dissolved in a mixture of chloroform:methanol (70:30) (v/v) at a concentration of 1 mg ml^{-1} and cholesterol which was dissolved in chloroform at a concentration of 20 mg ml ml^{-1}. All stock solutions were stored at −20°C in amber vials (Sigma-Aldrich, France).

Gold nanorods
Streptavidin-conjugated gold nanorods (C12-10-850-TS-DIH-50) were purchased from Nanopartz™. They have a peak of absorption at λ=834 nm, with a tail spanning the wavelength of the optical tweezers (λ=1064 nm). The stock solution (typical concentration 1750 ppm) was diluted 1:100 upon incubation with GUVs and again diluted 1:40 when GUVs were transferred to the observation chamber.

Lipid mixture preparation
Lipid stock solutions were mixed to obtain the desired molar ratio of EPC:DOPS:DOPE:cholesterol:PI(4,5)P2/DSPE-PEG2000-Biotin:PE–Rhodamine (50.7:10:10:15:10:0.2:0.1) at a total concentration of 1 mg/ml in chloroform. For binding experiments, we also used EPC:DOPS:DOPE:cholesterol:DSPE-PEG2000-Biotin:PE–Rhodamine (50.7:20:10:15:0.2:0.1) as a comparison. After use, argon was added to the vials before sealing them with paraffin film (Parafilm) to prevent lipid oxidation.

GUV preparation – PVA gel-assisted swelling
All GUVs used in this study were prepared by spontaneous swelling of polyvinyl alcohol (PVA)-based gels (Weinberger et al., 2013). PVA gel (5% PVA, 50 mM Sucrose, 25 mM NaCl and 25 mM Tris-HCl, at pH 7.4) was deposited on plasma cleaned (PDC-32G, Harrick) glass coverslips (18×18 mm, VWR International, France). The excess gel was removed. The glass cover slides were then dried for 50 min at 60°C. 15 μl of lipid solutions at 1 mg/ml were deposited on the PVA-coated slides by using a Hamilton syringe to make a dry lipid film as thin as possible. To remove

residual solvent, the lipid film was further dried under vacuum for 20 min at room temperature. The lipid film is then rehydrated with the growth buffer at room temperature. Vesicles formed within ~60 min and were extracted by pipetting directly from the slides.

Protein–GUV binding assay – spinning disk observation
GUVs collected after gel-assisted growth were then incubated 15 min with CHMP proteins at 500 nM in the observation buffer (50 mM NaCl and 25 mM Tris-HCl, at pH 7.4) with an osmolarity equal to that of the growth buffer (Vapor Pressure Osmometer, ELITechGroup WESCOR). Fluorodish cell culture dishes (35 mm with a 23 mm well; World Precision Instruments Inc., Germany) were used for the protein–GUV binding assay observation. Before use, the dishes were passivated with a 5 mg/ml β-casein solution (100 mM NaCl and 25 mM Tris-HCl pH 7.4) for 15 min to prevent GUVs and CHMP proteins from adhering to the glass surface. The dishes were then rinsed and filled with the observation buffer. GUVs were observed with a spinning disk confocal microscope equipped on an inverted Nikon Eclipse Ti-E microscope with 100× oil objective. Images were recorded with an EM-CCD Evolve camera. The exposure time for all images was 50 ms.

Protein-membrane binding assay – FACS
GUVs collected after gel-assisted growth were incubated 30 min with CHMP proteins at different concentrations in the observation buffer (50 mM NaCl and 25 mM Tris-HCl pH 7.4) with an osmolarity equal to that of the growth buffer (Vapor Pressure Osmometer, ELITechGroup WESCOR). The fluorescence intensity of GUVs and CHMPs was measured with a BD LSRFORTESSA flow cytometry instrument. Data analysis was performed with BD FACS Diva software.

Protein diffusion assay – FRAP
GUVs collected after electroformation growth were incubated with CHMP proteins at 500 nM in the observation buffer (50 mM NaCl and 25 mM Tris-HCl pH 7.4) for 30 min. Fluorodish cell culture was used for the protein diffusion assay. Before passivating the dishes with β-casein, they were coated with streptavidin at 10 μm/ml for 30 min, to avoid vesicle rotation, which would lead to an artifact in measuring the recovery. In order to avoid recovery from soluble protein in the GUV external solution, samples were diluted in the observation buffer upon imaging. For the FRAP experiments on the GUVs, an inverted spinning disk confocal Roper/Nikon microscope with a FRAP/Photo Activation module with a 60× oil objective was used. Images were recorded with an EM-CCD Evolve camera. Bleaching was performed along the z-axis, resulting in bleaching of a sector of the GUV. The typical arc length of such sector was 5 μm. Quantification was performed on a single GUV plane. Large error bars are due both to the intrinsic low fluorescence of the nanotube (causing a low signal to noise ratio) and to the fluctuation of the nanotube across the focal plane during prolonged imaging.

Measurement of protein density at GUV surface
We measured the protein signal at GUV surface by performing a line-scan measurement using Fiji, as shown in Fig. S4B,C. The values obtained were averaged and compared to standard curve of Alexa Fluor 488 or Alexa Fluor 647 for CHMP2B-ΔC and CHMP2A-ΔC, respectively. The dye intensities on GUV surface correspond to bulk concentrations ≈4 μM (for Alexa Fluor 488) and ≈18 μM (for Alexa Fluor 647). Given a protein labeling efficiency of 95% and 78%, respectively, this results in a protein density six times lower for CHMP2B-ΔC than for CHMP2A-ΔC.

Streptavidin diffusion assay – FRAP
GUVs collected after gel-assisted growth were incubated with CHMP proteins at 500 nM in the observation buffer (50 mM NaCl and 25 mM Tris-HCl pH 7.4) for duration of 30 min to reach saturation of the protein on the membrane. An inverted spinning disk confocal Roper/Nikon microscope with a FRAP/photo activation module is used for the FRAP experiments. For all series of FRAP experiments, we bleached the region of interest. Bleaching was performed along the z-axis, resulting in bleaching of a sector of the GUV. The typical arc length of such sectors was 5 μm. Quantification was performed on a single GUV plane.

GUV growth, washing and incubation with nanorods for tube pulling experiments

250 µl of GUVs extracted from each PVA slide was mixed with 1250 µl of external buffer and centrifuged for 10 min at 1000 *g*. 10 µl of GUVs taken from the bottom of the Eppendorf were mixed with 90 µl of external buffer plus 0.75 µl of gold nanorods and incubated for 20 min at room temperature. 10 µl of GUVs taken from the bottom of the Eppendorf were added to the imaging chamber, having a total volume of 200 µl. Thus, the protein present outside the GUVs is diluted 1200-fold, dropping from the initial nominal concentration of 2 µM to a concentration <2 nM.

Measurement of CHMP2B-ΔC concentration after encapsulation inside a GUV

CHMP2B-ΔC–Alexa-Fluor-488 was mixed with growth buffer (Table 1) at an initial concentration of 2 µM. Vesicles collected from the PVA slides were imaged in comparison to a standard curve of Alexa Fluor 488. The dye concentration after encapsulation is ≈270 nM. As protein labeling efficiency is 95%, this results in a concentration of encapsulated CHMP2B-ΔC of ≈250 nM.

Tube experiments

Our set-up has been previously described (Prévost et al., 2015). It comprises a Nikon C1 confocal microscope equipped with optical tweezers and micromanipulators. Micropipettes were used to manipulate individual GUVs and control their tension. Before the experiment, the chamber and the micropipettes were passivated with β-casein (5 mg/ml). After 15 min, the β-casein solution was replaced with the external buffer (Table 1). 5 µl of each population of GUVs (previously incubated with gold nanorods) and 2 µl of streptavidin-coated beads were then added. A bead was aspirated and held with one micropipette, while two GUVs were aspirated in the other micropipettes and were held under low tension. A nanotube was pulled from the PI(4,5)P2-containing GUV, and the GUVs were brought into contact at the position of the position of the optical tweezers. Instantaneous fusion was seen once the optical tweezers was activated. After fusion and binding, tension was gradually increased. At each step, one fluorescence image was acquired (at the end of a 2-min period to allow equilibration). When possible, these steps were reversed until a minimal tension was again reached. The values of tube radius given in this article were deduced from the fluorescence intensity of the tube in comparison with the fluorescence of the GUV, as described previously (Prévost et al., 2015). For the quantification of CHMP2B localization at neck, measurements were binned according to the tube diameter, and the presence or absence of a CHMP2B cluster at neck was manually scored. The percentage of necks with stable cluster localization for each tube diameter is indicated in the quantification.

References

Adell, M. A. Y., Migliano, S. M., Upadhyayula, S., Bykov, Y. S., Sprenger, S., Pakdel, M., Vogel, G. F., Jih, G., Skillern, W., Behrouzi, R. et al. (2017). Recruitment dynamics of ESCRT-III and Vps4 to endosomes and implications for reverse membrane budding. *eLife* **6**, e31652.

Adrian, M., Kusters, R., Wierenga, C. J., Storm, C., Hoogenraad, C. C. and Kapitein, L. C. (2014). Barriers in the brain: resolving dendritic spine morphology and compartmentalization. *Front. Neuroanat.* **8**, 142.

Agromayor, M. and Martin-Serrano, J. (2013). Knowing when to cut and run: mechanisms that control cytokinetic abscission. *Trends Cell Biol.* **23**, 433-441.

Aimon, S., Callan-Jones, A., Berthaud, A., Pinot, M., Toombes, G. E. and Bassereau, P. (2014). Membrane shape modulates transmembrane protein distribution. *Dev. Cell* **28**, 212-218.

Alonso Y Adell, M., Migliano, S. M. and Teis, D. (2016). ESCRT-III and Vps4: a dynamic multipurpose tool for membrane budding and scission. *FEBS J.* **283**, 3288-3302.

Arellano, J. I., Benavides-Piccione, R., Defelipe, J. and Yuste, R. (2007). Ultrastructure of dendritic spines: correlation between synaptic and spine morphologies. *Front. Neurosci.* **1**, 131-143.

Baumgärtel, V., Ivanchenko, S., Dupont, A., Sergeev, M., Wiseman, P. W., Kräusslich, H. G., Bräuchle, C., Müller, B. and Lamb, D. C. (2011). Live-cell visualization of dynamics of HIV budding site interactions with an ESCRT component. *Nat. Cell Biol.* **13**, 469-474.

Belly, A., Bodon, G., Blot, B., Bouron, A., Sadoul, R. and Goldberg, Y. (2010). CHMP2B mutants linked to frontotemporal dementia impair maturation of dendritic spines. *J. Cell Sci.* **123**, 2943-2954.

Bodon, G., Chassefeyre, R., Pernet-Gallay, K., Martinelli, N., Effantin, G., Hulsik, D. L., Belly, A., Goldberg, Y., Chatellard-Causse, C., Blot, B. et al. (2011). Charged multivesicular body protein 2B (CHMP2B) of the endosomal sorting complex required for transport-III (ESCRT-III) polymerizes into helical structures deforming the plasma membrane. *J. Biol. Chem.* **286**, 40276-40286.

Buchkovich, N. J., Henne, W. M., Tang, S. and Emr, S. D. (2013). Essential N-terminal insertion motif anchors the ESCRT-III filament during MVB vesicle formation. *Dev. Cell* **27**, 201-214.

Campillo, C., Sens, P., Koster, D., Pontani, L. L., Levy, D., Bassereau, P., Nassoy, P. and Sykes, C. (2013). Unexpected membrane dynamics unveiled by membrane nanotube extrusion. *Biophys. J.* **104**, 1248-1256.

Chassefeyre, R., Martinez-Hernandez, J., Bertaso, F., Bouquier, N., Blot, B., Laporte, M., Fraboulet, S., Coute, Y., Devoy, A., Isaacs, A. M. et al. (2015). Regulation of postsynaptic function by the dementia-related ESCRT-III subunit CHMP2B. *J. Neurosci.* **35**, 3155-3173.

Chiaruttini, N., Redondo-Morata, L., Colom, A., Humbert, F., Lenz, M., Scheuring, S. and Roux, A. (2015). Relaxation of loaded ESCRT-III spiral springs drives membrane deformation. *Cell* **163**, 866-879.

Christ, L., Raiborg, C., Wenzel, E. M., Campsteijn, C. and Stenmark, H. (2017). Cellular functions and molecular mechanisms of the ESCRT membrane-scission machinery. *Trends Biochem. Sci.* **42**, 42-56.

Di Paolo, G. and De Camilli, P. (2006). Phosphoinositides in cell regulation and membrane dynamics. *Nature* **443**, 651-657.

Domanov, Y. A., Aimon, S., Toombes, G. E., Renner, M., Quemeneur, F., Triller, A., Turner, M. S. and Bassereau, P. (2011). Mobility in geometrically confined membranes. *Proc. Natl. Acad. Sci. USA* **108**, 12605-12610.

Ewers, H., Tada, T., Petersen, J. D., Racz, B., Sheng, M. and Choquet, D. (2014). A septin-dependent diffusion barrier at dendritic spine necks. *PLoS ONE* **9**, e113916.

Garnier-Lhomme, M., Byrne, R. D., Hobday, T. M., Gschmeissner, S., Woscholski, R., Poccia, D. L., Dufourc, E. J. and Larijani, B. (2009). Nuclear envelope remnants: fluid membranes enriched in sterols and polyphosphoinositides. *PLoS ONE* **4**, e4255.

Ghazi-Tabatabai, S., Saksena, S., Short, J. M., Pobbati, A. V., Veprintsev, D. B., Crowther, R. A., Emr, S. D., Egelman, E. H. and Williams, R. L. (2008).

Structure and disassembly of filaments formed by the ESCRT-III subunit Vps24. *Structure* **16**, 1345-1356.

Grutzendler, J., Kasthuri, N. and Gan, W. B. (2002). Long-term dendritic spine stability in the adult cortex. *Nature* **420**, 812-816.

Guizetti, J. and Gerlich, D. W. (2012). ESCRT-III polymers in membrane neck constriction. *Trends Cell Biol.* **22**, 133-140.

Heinemann, F., Vogel, S. K. and Schwille, P. (2013). Lateral membrane diffusion modulated by a minimal actin cortex. *Biophys. J.* **104**, 1465-1475.

Henne, W. M., Buchkovich, N. J., Zhao, Y. and Emr, S. D. (2012). The endosomal sorting complex ESCRT-II mediates the assembly and architecture of ESCRT-III helices. *Cell* **151**, 356-371.

Henne, W. M., Stenmark, H. and Emr, S. D. (2013). Molecular mechanisms of the membrane sculpting ESCRT pathway. *Cold Spring Harbor Perspect. Biol.* **5**, a016766.

Horger, K. S., Estes, D. J., Capone, R. and Mayer, M. (2009). Films of agarose enable rapid formation of giant liposomes in solutions of physiologic ionic strength. *J. Am. Chem. Soc.* **131**, 1810-1819.

Horne, E. A. and Dell'acqua, M. L. (2007). Phospholipase C is required for changes in postsynaptic structure and function associated with NMDA receptor-dependent long-term depression. *J. Neurosci.* **27**, 3523-3534.

Hu, Q., Milenkovic, L., Jin, H., Scott, M. P., Nachury, M. V., Spiliotis, E. T. and Nelson, W. J. (2010). A septin diffusion barrier at the base of the primary cilium maintains ciliary membrane protein distribution. *Science* **329**, 436-439.

Jalmar, O., García-Sáez, A. J., Berland, L., Gonzalvez, F. and Petit, P. X. (2010). Giant unilamellar vesicles (GUVs) as a new tool for analysis of caspase-8/Bid-FL complex binding to cardiolipin and its functional activity. *Cell Death Dis.* **1**, e103.

Jimenez, A. J., Maiuri, P., Lafaurie-Janvore, J., Divoux, S., Piel, M. and Perez, F. (2014). ESCRT machinery is required for plasma membrane repair. *Science* **343**, 1247136.

Jouvenet, N., Zhadina, M., Bieniasz, P. D. and Simon, S. M. (2011). Dynamics of ESCRT protein recruitment during retroviral assembly. *Nat. Cell Biol.* **13**, 394-401.

Juan, T. and Fürthauer, M. (2018). Biogenesis and function of ESCRT-dependent extracellular vesicles. *Semin. Cell Dev. Biol.* **74**, 66-77.

Lata, S., Roessle, M., Solomons, J., Jamin, M., Gőttlinger, H. G., Svergun, D. I. and Weissenhorn, W. (2008a). Structural basis for autoinhibition of ESCRT-III CHMP3. *J. Mol. Biol.* **378**, 818-827.

Lata, S., Schoehn, G., Jain, A., Pires, R., Piehler, J., Gottlinger, H. G. and Weissenhorn, W. (2008b). Helical structures of ESCRT-III are disassembled by VPS4. *Science* **321**, 1354-1357.

Lattante, S., Ciura, S., Rouleau, G. A. and Kabashi, E. (2015). Defining the genetic connection linking amyotrophic lateral sclerosis (ALS) with frontotemporal dementia (FTD). *Trends Genet.* **31**, 263-273.

Lee, I. H., Kai, H., Carlson, L. A., Groves, J. T. and Hurley, J. H. (2015). Negative membrane curvature catalyzes nucleation of endosomal sorting complex required for transport (ESCRT)-III assembly. *Proc. Natl. Acad. Sci. USA* **112**, 15892-15897.

Lendvai, B., Zelles, T., Rozsa, B. and Vizi, E. S. (2003). A vinca alkaloid enhances morphological dynamics of dendritic spines of neocortical layer 2/3 pyramidal cells. *Brain Res. Bull.* **59**, 257-260.

Leung, K. F., Dacks, J. B. and Field, M. C. (2008). Evolution of the multivesicular body ESCRT machinery; retention across the eukaryotic lineage. *Traffic* **9**, 1698-1716.

Mccullough, J., Clippinger, A. K., Talledge, N., Skowyra, M. L., Saunders, M. G., Naismith, T. V., Colf, L. A., Afonine, P., Arthur, C., Sundquist, W. I. et al. (2015). Structure and membrane remodeling activity of ESCRT-III helical polymers. *Science* **350**, 1548-1551.

Meleard, P., Bagatolli, L. A. and Pott, T. (2009). Giant unilamellar vesicle electroformation from lipid mixtures to native membranes under physiological conditions. *Methods Enzymol.* **465**, 161-176.

Mierzwa, B. E., Chiaruttini, N., Redondo-Morata, L., Von Filseck, J. M., Konig, J., Larios, J., Poser, I., Muller-Reichert, T., Scheuring, S., Roux, A. et al. (2017). Dynamic subunit turnover in ESCRT-III assemblies is regulated by Vps4 to mediate membrane remodeling during cytokinesis. *Nat. Cell Biol.* **19**, 787-798.

Muziol, T., Pineda-Molina, E., Ravelli, R. B., Zamborlini, A., Usami, Y., Göttlinger, H. and Weissenhorn, W. (2006). Structural basis for budding by the ESCRT-III factor CHMP3. *Dev. Cell* **10**, 821-830.

Olmos, Y. and Carlton, J. G. (2016). The ESCRT machinery: new roles at new holes. *Curr. Opin. Cell Biol.* **38**, 1-11.

Pires, R., Hartlieb, B., Signor, L., Schoehn, G., Lata, S., Roessle, M., Moriscot, C., Popov, S., Hinz, A., Jamin, M. et al. (2009). A crescent-shaped ALIX dimer targets ESCRT-III CHMP4 filaments. *Structure* **17**, 843-856.

Pontani, L. L., Van Der Gucht, J., Salbreux, G., Heuvingh, J., Joanny, J. F. and Sykes, C. (2009). Reconstitution of an actin cortex inside a liposome. *Biophys. J.* **96**, 192-198.

Prévost, C., Zhao, H., Manzi, J., Lemichez, E., Lappalainen, P., Callan-Jones, A. and Bassereau, P. (2015). IRSp53 senses negative membrane curvature and phase separates along membrane tubules. *Nat. Commun.* **6**, 8529.

Rørvig-Lund, A., Bahadori, A., Semsey, S., Bendix, P. M. and Oddershede, L. B. (2015). Vesicle fusion triggered by optically heated gold nanoparticles. *Nano Lett.* **15**, 4183-4188.

Sadoul, R., Laporte, M. H., Chassefeyre, R., Chi, K. I., Goldberg, Y., Chatellard, C., Hemming, F. J. and Fraboulet, S. (2018). The role of ESCRT during development and functioning of the nervous system. *Semin. Cell Dev. Biol.* **74**, 40-49.

Schlimpert, S., Klein, E. A., Briegel, A., Hughes, V., Kahnt, J., Bolte, K., Maier, U. G., Brun, Y. V., Jensen, G. J., Gitai, Z. et al. (2012). General protein diffusion barriers create compartments within bacterial cells. *Cell* **151**, 1270-1282.

Scourfield, E. J. and Martin-Serrano, J. (2017). Growing functions of the ESCRT machinery in cell biology and viral replication. *Biochem. Soc. Trans.* **45**, 613-634.

Shah, M. M., Hammond, R. S. and Hoffman, D. A. (2010). Dendritic ion channel trafficking and plasticity. *Trends Neurosci.* **33**, 307-316.

Shen, Q. T., Schuh, A. L., Zheng, Y., Quinney, K., Wang, L., Hanna, M., Mitchell, J. C., Otegui, M. S., Ahlquist, P., Cui, Q. et al. (2014). Structural analysis and modeling reveals new mechanisms governing ESCRT-III spiral filament assembly. *J. Cell Biol.* **206**, 763-777.

Shim, S., Kimpler, L. A. and Hanson, P. I. (2007). Structure/function analysis of four core ESCRT-III proteins reveals common regulatory role for extreme C-terminal domain. *Traffic* **8**, 1068-1079.

Skibinski, G., Parkinson, N. J., Brown, J. M., Chakrabarti, L., Lloyd, S. L., Hummerich, H., Nielsen, J. E., Hodges, J. R., Spillantini, M. G., Thusgaard, T. et al. (2005). Mutations in the endosomal ESCRTIII-complex subunit CHMP2B in frontotemporal dementia. *Nat. Genet.* **37**, 806-808.

Sorre, B., Callan-Jones, A., Manzi, J., Goud, B., Prost, J., Bassereau, P. and Roux, A. (2012). Nature of curvature coupling of amphiphysin with membranes depends on its bound density. *Proc. Natl. Acad. Sci. USA* **109**, 173-178.

Tang, S., Henne, W. M., Borbat, P. P., Buchkovich, N. J., Freed, J. H., Mao, Y., Fromme, J. C. and Emr, S. D. (2015). Structural basis for activation, assembly and membrane binding of ESCRT-III Snf7 filaments. *Elife* **4**, e12548.

Teis, D., Saksena, S. and Emr, S. D. (2008). Ordered assembly of the ESCRT-III complex on endosomes is required to sequester cargo during MVB formation. *Dev. Cell* **15**, 578-589.

Trachtenberg, J. T., Chen, B. E., Knott, G. W., Feng, G., Sanes, J. R., Welker, E. and Svoboda, K. (2002). Long-term in vivo imaging of experience-dependent synaptic plasticity in adult cortex. *Nature* **420**, 788-794.

Trimble, W. S. and Grinstein, S. (2015). Barriers to the free diffusion of proteins and lipids in the plasma membrane. *J. Cell Biol.* **208**, 259-271.

Van Der Zee, J., Urwin, H., Engelborghs, S., Bruyland, M., Vandenberghe, R., Dermaut, B., De Pooter, T., Peeters, K., Santens, P., De Deyn, P. P. et al. (2008). CHMP2B C-truncating mutations in frontotemporal lobar degeneration are associated with an aberrant endosomal phenotype in vitro. *Hum. Mol. Genet.* **17**, 313-322.

Visco, I., Hoege, C., Hyman, A. A. and Schwille, P. (2016). In vitro reconstitution of a membrane switch mechanism for the polarity protein LGL. *J. Mol. Biol.* **428**, 4828-4842.

Votteler, J. and Sundquist, W. I. (2013). Virus budding and the ESCRT pathway. *Cell Host Microbe* **14**, 232-241.

Wang, L., Dumoulin, A., Renner, M., Triller, A. and Specht, C. G. (2016). The role of synaptopodin in membrane protein diffusion in the dendritic spine neck. *PLoS ONE* **11**, e0148310.

Weinberger, A., Tsai, F.-C., Koenderink, G. H., Schmidt, T. F., Itri, R., Meier, W., Schmatko, T., Schröder, A. and Marques, C. (2013). Gel-assisted formation of giant unilamellar vesicles. *Biophys. J.* **105**, 154-164.

Weissenhorn, W., Poudevigne, E., Effantin, G. and Bassereau, P. (2013). How to get out: ssRNA enveloped viruses and membrane fission. *Curr. Opin. Virol.* **3**, 159-167.

Xiao, J., Chen, X.-W., Davies, B. A., Saltiel, A. R., Katzmann, D. J. and Xu, Z. (2009). Structural basis of Ist1 function and Ist1-Did2 interaction in the multivesicular body pathway and cytokinesis. *Mol. Biol. Cell* **20**, 3514-3524.

Yang, G., Pan, F. and Gan, W. B. (2009). Stably maintained dendritic spines are associated with lifelong memories. *Nature* **462**, 920-924.

Yasuda, R. (2017). Biophysics of biochemical signaling in dendritic spines: implications in synaptic plasticity. *Biophys. J.* **113**, 2152-2159.

Zamborlini, A., Usami, Y., Radoshitzky, S. R., Popova, E., Palu, G. and Gottlinger, H. (2006). Release of autoinhibition converts ESCRT-III components into potent inhibitors of HIV-1 budding. *Proc. Natl. Acad. Sci. USA* **103**, 19140-19145.